RESEARCH ARTICLE | DECEMBER 23 2024

# Excited state properties from the Bethe–Salpeter equation: State-to-state transitions and spin–orbit coupling

Paula Himmelsbach ; Christof Holzer



*J. Chem. Phys.* 161, 244105 (2024)
https://doi.org/10.1063/5.0244254

The Journal of Chemical Physics ARTICLE pubs.aip.org/aip/jcp

# Excited state properties from the Bethe–Salpeter equation: State-to-state transitions and spin–orbit coupling

Cite as: J. Chem. Phys. 161, 244105 (2024); doi: 10.1063/5.0244254
Submitted: 17 October 2024 • Accepted: 5 December 2024 •
Published Online: 23 December 2024



Paula Himmelsbach and Christof Holzer[a)]

## AFFILIATIONS

Institute of Theoretical Solid State Physics, Karlsruhe Institute of Technology, Kaiserstraße 12, 76131 Karlsruhe, Germany

[a)]Author to whom correspondence should be addressed: holzer@kit.edu

## ABSTRACT

The formalism to calculate excited state properties from the *GW*–Bethe–Salpeter equation (BSE) method is introduced, providing convenient access to excited state absorption, excited state circular dichroism, and excited state optical rotation in the framework of the *GW*–BSE method. This is achieved using the second-order transition density, which can be obtained by solving a set of auxiliary equations similar to time-dependent density functional theory (TD-DFT). The proposed formulation therefore leads to no increase in the formal computational complexity when compared to the corresponding ground state properties. We further outline the calculation of fully relaxed spin–orbit coupling matrix elements within the *GW*–BSE method, allowing us to include perturbative corrections for spin–orbit coupling in aforementioned properties. These corrections are also extended to TD-DFT. Excited state absorption and perturbative spin–orbit coupling corrections within *GW*–BSE are evaluated for a selected set of molecular systems, yielding promising results.





## I. INTRODUCTION

Recently, analytic implementations of excited state properties from the *GW*–Bethe–Salpeter equation (BSE) method have surged in the literature. For example, excited state dipole moments,[1] nonlinear optical properties as hyperpolarizabilities, and two-photon absorption have become available in the framework of the *GW*–BSE method[2] and approximate Lagrangian Z-vector methods related to excited state geometry optimizations.[3] Going beyond the simple calculation of excited state energies and oscillator strengths is an important task in the development of *GW*–BSE, leading to one of the final domains where time-dependent density functional theory (TD-DFT) is more versatile than *GW*–BSE due to the lack of available implementations of the latter. This situation is unsatisfactory given the excellent performance of *GW*–BSE for both local and charge-transfer excited states.[4–9] Recent advances within the *GW*–BSE method further outline the possibility to perform frequency-dependent simulations[10–12] and other ways to recover double excitations.[13]

In this work, we will therefore introduce the formalism required to perform calculations on excited state properties within the framework of the *GW*–BSE method. Examples of the accessible properties include excited state absorption, excited state circular dichroism, and excited state optical rotation. We will focus on the static screened BSE,[6] and note that an extension to dynamic BSE methods[10–12] is in principle possible, but not straightforward. Given the high similarity of the required intermediates, we will also outline a way to perturbatively include spin–orbit coupling (SOC) in these properties in both the ground and excited states. This allows for a convenient evaluation of these properties at the *GW*–BSE level of theory, encouraging this powerful method to prosper in fields that have been out of reach before. We will additionally use the opportunity to introduce spin–orbit coupling matrix elements (SOCMEs) in a less incorrect way than previous TD-DFT implementations[14–17] and put them more in line with previous studies on multiconfigurational linear response functions.[18] Combining the possibility to access excited state properties and spin–orbit coupling (SOC), we will finally outline the capabilities and performance of the newly developed method for four selected sizable molecular systems. Favorable aspects as well as caveats of the *GW*–BSE method for excited state properties and perturbative spin–orbit coupling for these systems will subsequently be discussed.

## II. THEORY

### A. State-to-state transitions in the framework of the *GW*–Bethe–Salpeter equation method

Similar to TD-DFT, excitation energies can be extracted from the poles of the symplectic BSE eigenvalue problem,[19–23]

$$[(\mathbf{A}-\mathbf{B})(\mathbf{A}+\mathbf{B})]\mathbf{R}^N = \omega_N^2 \mathbf{R}^N, \tag{1}$$

$$[(\mathbf{A}+\mathbf{B})(\mathbf{A}-\mathbf{B})]\mathbf{L}^N = \omega_N^2 \mathbf{L}^N. \tag{2}$$

Within the static screened BSE, the matrices $(\mathbf{A}+\mathbf{B})$ and $(\mathbf{A}-\mathbf{B})$ are defined as

$$(A+B)_{ia,jb} = (\varepsilon_a - \varepsilon_i)\delta_{ab}\delta_{ij} + H^+_{ai,bj}, \tag{3}$$

$$(A-B)_{ia,jb} = H^-_{ai,bj}. \tag{4}$$

The solutions $\mathbf{R} = (\mathbf{X}+\mathbf{Y})$ and $\mathbf{L} = (\mathbf{X}-\mathbf{Y})$ are normalized to obey the relation

$$\langle R^N | L^M \rangle = \delta_{NM}. \tag{5}$$

This partition is useful, as after a unitary transformation into the real atomic orbital (AO) basis, the matrices $(\mathbf{A}+\mathbf{B})$ and $\mathbf{R}$ are symmetric, while $(\mathbf{A}-\mathbf{B})$ and $\mathbf{L}$ are skew-symmetric.[24,25] Equations (3) and (4) have introduced the two-electron kernel contributions,

$$H^{+,\mathrm{BSE}}_{pq,rs} = v_{pq,rs} - W_{ps,qr}(\omega=0) - W_{pr,qs}(\omega=0), \tag{6}$$

$$H^{-,\mathrm{BSE}}_{pq,rs} = W_{ps,qr}(\omega=0) - W_{pr,qs}(\omega=0), \tag{7}$$

with $v_{pq,rs}$ being a Coulomb integral and $\mathbf{W}(\omega)$ denoting the screened exchange. The latter is obtained from $\mathbf{v}$ and the inverse of the dielectric function $\boldsymbol{\kappa}$,

$$W_{pq,rs}(\omega) = \sum_{tu} \kappa^{-1}_{pq,tu}(\omega) v_{tu,rs}. \tag{8}$$

Efficient procedures to evaluate Eq. (8) for arbitrary values of $\omega$ have been outlined in the literature.[23,26] To emphasize the similarity between the BSE and TD-DFT, we note that the latter simply replaces the kernels with

$$H^{+,\mathrm{DFT}}_{pq,rs} = v_{pq,rs} + f^{\mathrm{XC,sy}}_{ps,qr}, \tag{9}$$

$$H^{-,\mathrm{DFT}}_{pq,rs} = f^{\mathrm{XC,as}}_{pr,qs}. \tag{10}$$

Similar to DFT[27] and the calculation of two-photon absorption and hyperpolarizabilities in the framework of the BSE,[2] a state-to-state transition within the BSE can be calculated from the double residue of the quadratic response function,

$$v_{NM} = \lim_{\omega_\eta \to -\Omega_N} (\omega_\eta + \Omega_N) \lim_{\omega_\theta \to \Omega_M} (\omega_\theta - \Omega_M) \times \langle\langle v^\zeta; v^\eta(\omega_\eta), v^\theta(\omega_\theta)\rangle\rangle = \mathrm{Tr}\left(\hat{v}^\zeta \gamma^{NM}\right), \tag{11}$$

where $\gamma^{NM}$ is the state-to-state transition density matrix. As it constitutes a single determinant method, $\gamma^{NM}$ can be obtained from the idempotency constraint of the time-dependent Kohn–Sham determinant as[28]

$$\gamma^0 = \gamma^0\gamma^0, \tag{12}$$

$$\gamma^N = \gamma^0\gamma^N + \gamma^N\gamma^0, \tag{13}$$

$$\gamma^{NM} = \gamma^0\gamma^{NM} + \gamma^N\gamma^M + \gamma^M\gamma^N + \gamma^{NM}\gamma^0. \tag{14}$$

Given the independence of the density matrix from the actual eigenvalues, Eq. (12) holds true for common *GW* methods, as for example the $G_0W_0$ method, but also for the eigenvalue and quasiparticle self-consistent ev*GW* and qs*GW* variants.[29,30] Inserting the definitions of $\gamma^0$ and $\gamma^N$,

$$\gamma^0(x,x') = \sum_j \phi_j(x)\phi_j^*(x'), \tag{15}$$

$$\gamma^N(x,x') = \sum_{bj} \left[X^N_{jb}\phi_b(x)\phi_j^*(x') + Y^N_{jb}\phi_j(x)\phi_b^*(x')\right], \tag{16}$$

as determined from the ground state Kohn–Sham equations $(\phi_j)$ and linear response $(\{X,Y\})$ leads to the matrix form

$$\gamma^{NM} = \begin{pmatrix} K^{NM}_{ij} & X^{NM}_{ib} \\ Y^{NM}_{aj} & K^{NM}_{ab} \end{pmatrix}, \tag{17}$$

of the second-order transition density $\gamma^{NM}$. Equation (17) closely resembles the corresponding quantities in Refs. 2 and 27. Note that $\gamma^{NM}$ differs from the second-order single-particle reduced BSE density matrix of Ref. 2 by replacing the perturbations $\{\eta,\zeta\}$ with the excited states $\{N,M\}$. Notably, the matrix elements are calculated slightly differently, too. As indicated in Eq. (11), a switch of sign has taken place for the excitation.[27] Instead of the eigenpair $\omega_M, \{\mathbf{X},\mathbf{Y}\}$, the time-reversal symmetry related eigenpair $-\omega_M, \{\mathbf{Y}^*,\mathbf{X}^*\}$ is to be used. For purely real orbitals, this manifests in a change of sign of $\mathbf{L}^M$. This change of sign must be accounted for in subsequent evaluations of the matrix elements of $\gamma^{NM}$. The diagonal subblocks of Eq. (17) are obtained in a straightforward manner as products of linear response vectors

$$K^{NM,+}_{ij} = -\frac{1}{4}\sum_a \left[R^N_{ia}R^M_{ja} + L^M_{ia}L^N_{ja} + (N \leftrightarrow M)\right], \tag{18}$$

$$K^{NM,-}_{ij} = \frac{1}{4}\sum_a \left[L^N_{ia}R^M_{ja} + R^N_{ia}L^M_{ja} - (N \leftrightarrow M)\right], \tag{19}$$

$$K^{NM,+}_{ab} = \frac{1}{4}\sum_i \left[R^N_{ia}R^M_{ib} + L^N_{ia}L^M_{ib} + (N \leftrightarrow M)\right], \tag{20}$$

$$K^{NM,-}_{ab} = \frac{1}{4}\sum_i \left[L^N_{ia}R^M_{ib} + R^N_{ia}L^M_{ib} - (N \leftrightarrow M)\right], \tag{21}$$

arising from the second and third terms on the right-hand side of Eq. (14). $\mathbf{R}$ and $\mathbf{L}$ are solutions of the linear response equations

for the excited states $N$ and $M$, where the time-reversal symmetric partner of the excitation $M$ is to be used.

The off-diagonal blocks $X_{ib}^{NM}$ and $Y_{aj}^{NM}$ require the solution of the second-order Bethe–Salpeter response equations. Again using the symmetry adapted linear combinations $\mathbf{R}^{NM} = \left(\mathbf{X}^{NM} + \mathbf{Y}^{NM}\right)$ and $\mathbf{L}^{NM} = \left(\mathbf{X}^{NM} - \mathbf{Y}^{NM}\right)$, these equations read

$$\left[(\mathbf{A}-\mathbf{B})(\mathbf{A}+\mathbf{B}) - \omega_\zeta^2 \mathbf{1}\right]\mathbf{R}^{NM} = \mathbf{U}^{NM}, \tag{22}$$

$$\left[(\mathbf{A}+\mathbf{B})(\mathbf{A}-\mathbf{B}) - \omega_\zeta^2 \mathbf{1}\right]\mathbf{L}^{NM} = \mathbf{V}^{NM}. \tag{23}$$

The right-hand side (RHS) of Eqs. (22) and (23) is defined as

$$\begin{aligned} U_{ia}^{NM} = &-\frac{1}{2}\sum_j \left[R_{ja}^M M_{ij}^N + L_{ja}^M N_{ij}^N + (N \leftrightarrow M)\right] \\ &+ \frac{1}{2}\sum_b \left[R_{ib}^M M_{ab}^N + L_{ib}^M N_{ab}^N + (N \leftrightarrow M)\right] \\ &+ H_{ia}^+[K_{kl}^{NM,+}] + H_{ia}^+[K_{cd}^{NM,+}] + g_{ia}^{sy}\left(R^N, R^M\right), \end{aligned} \tag{24}$$

$$\begin{aligned} V_{ia}^{NM} = &+\frac{1}{2}\sum_j \left[L_{ja}^M M_{ij}^N + R_{ja}^M N_{ij}^N - (N \leftrightarrow M)\right] \\ &- \frac{1}{2}\sum_b \left[L_{ib}^M M_{ab}^N + R_{ib}^M N_{ab}^N - (N \leftrightarrow M)\right] \\ &- H_{ia}^-[K_{kl}^{NM,-}] - H_{ia}^-[K_{cd}^{NM,-}] - g_{ia}^{as}\left(L^N, L^M\right). \end{aligned} \tag{25}$$

In Eqs. (24) and (25), the quantities $\mathbf{M}$ and $\mathbf{N}$ are defined as

$$M_{pq}^N = \sum_{rs} H_{pq,rs}^+ R_{rs}^N, \tag{26}$$

$$N_{pq}^N = \sum_{rs} H_{pq,rs}^- L_{rs}^N. \tag{27}$$

$g^{\mathrm{XC}}$ refers to the first hyperkernel. Within adiabatic TD-DFT, it is approximated as

$$g^{\mathrm{XC}}(x,x',x'') \approx \frac{\partial^3 E(\rho)}{\partial\rho(x)\partial\rho(x')\partial\rho(x'')}. \tag{28}$$

The hyperkernel in Eq. (28) is purely symmetric for the local density approximation (LDA) and generalized gradient approximation (GGA). Starting from metaGGAs, antisymmetric terms from the current density arise, leading to non-vanishing antisymmetric hyperkernel contributions in Eq. (25).[31,32] This holds true in cases of current-free[31] and current-carrying ground states.[33,34] Spin integration leads to the hyperkernel vanishing in cases where the states $N$ and $M$ have different spin symmetries. Within the BSE, the hyperkernel is approximated in a similar manner as the linear response kernel, for which the approximation

$$\frac{\partial GW}{\partial G} \approx W \tag{29}$$

is used.[3,21] Accordingly, we assume

$$g^{\mathrm{BSE}} = \frac{\partial^2 GW}{\partial G \partial G} \approx \frac{\partial W}{\partial G} \approx 0 \tag{30}$$

to be equally valid, resulting in no significant hyperkernel contribution from the BSE. This approximation has been shown to lead to negligible errors for the Lagrangian Z-vector equations, and we project this also being the case for excited state properties.[3] While we estimate this to be a good approximation in many cases, we issue a warning that it has been shown that the initial approximation of Eq. (29) can be troublesome when going beyond standard static screened $GW$–BSE for neutral excitations.[35,36] Therefore, in cases of applying the BSE with dynamic corrections, to charged excitations, or with higher order corrections, the use of Eq. (30) needs to be reconsidered.

Note that for hybrid TD-DFT/BSE methods, as for example the correlation-kernel augmented BSE,[37] both the DFT and (vanishing) BSE hyperkernel are formally required. An implementation of the correlation-kernel augmented BSE is, however, trivial once both non-linear implementations are available. The frequency of the electric field perturbation $\omega_\zeta$ is formally set to $(\Omega_N - \Omega_M)$ when solving the second-order Bethe–Salpeter response equations (22) and (23). This leads to a set of equations for each pair of states. Special precaution needs to be taken in case of an actual excited state being in the vicinity of this energy difference. In this case, adding a non-vanishing imaginary component can be used to guarantee numerical stability.[2] To partly reduce the computational complexity and also resolve issues with the pole structure, it has been suggested to simply set $\omega^\zeta = 0$ in a pseudo-wavefunction approach.[38,39] This is a valid approximation for differences $|\Omega_N - \Omega_M| \ll \Omega_1$, i.e., if the first excited state has a significantly higher energy than the energy difference between the excited states $N$ and $M$.

By inserting Eqs. (17) and (25) into Eq. (11), a state-to-state coupling matrix element of a symmetric operator can be evaluated as

$$v_{NM}^{\zeta,sy} = \mathrm{Tr}\left(v_{ij}^\zeta K_{ij}^{NM,+}\right) + \mathrm{Tr}\left(v_{ab}^\zeta K_{ab}^{NM,+}\right) + \mathrm{Tr}\left(v_{ia}^\zeta R_{ia}^{NM}\right). \tag{31}$$

The most prominent example of a symmetric operator $\hat{v}$ is the dipole operator,

$$v_{pq}^{\zeta,\mathrm{dip.}} = \langle\phi_p|\vec{r}_\zeta|\phi_q\rangle, \tag{32}$$

which, when used for states of the same multiplicity, will lead to the excited state transition dipole moment components.

## B. Spin–orbit coupling matrix elements

The coupling matrix elements for skew-symmetric operators can be obtained from the skew-symmetric part,

$$v_{NM}^{\zeta,as} = \mathrm{Tr}\left(v_{ij}^\zeta K_{ij}^{NM,-}\right) + \mathrm{Tr}\left(v_{ab}^\zeta K_{ab}^{NM,-}\right) + \mathrm{Tr}\left(v_{ia}^\zeta L_{ia}^{NM}\right). \tag{33}$$

The most important example in this work is the spin–orbit mean field (SOMF) operator,[40,41]

$$\begin{aligned} v_{pq}^{\zeta,\mathrm{SOMF}} = &\left(\phi_p\middle|h_1^\zeta\middle|\phi_q\right) + 2\sum_{r=1}^{\mathrm{occ.}}\left\{\left(\phi_r\phi_r\middle|h_2^\zeta\middle|\phi_p\phi_q\right)\right. \\ &\left. - \frac{3}{2}\left(\phi_p\phi_r\middle|h_2^\zeta\middle|\phi_r\phi_q\right) + \frac{3}{2}\left(\phi_r\phi_q\middle|h_2^\zeta\middle|\phi_p\phi_r\right)\right\}, \end{aligned} \tag{34}$$

with

$$h_1^\eta = \frac{1}{2c}\sum_K \frac{Z_K[\vec{r}_K \times \vec{p}]_\eta}{\vec{r}_K^3}, \tag{35}$$

$$h_2^\eta = \frac{1}{2c}\frac{[\vec{r} \times \vec{p}]_\eta}{\vec{r}^3}, \tag{36}$$

leading to the well-known spin–orbit coupling matrix elements (SOCMEs). The final term in Eq. (31) is not present in Eq. (33), as any skew-symmetric operator is traceless.

To arrive at previous results,[15–17] two approximations must be made in Eq. (33). First, the final term, yielding the orbital response, is neglected in previous studies. Second, the Tamm–Dancoff approximation needs to be applied also for full TD-DFT vectors, leading to the observed re-normalization necessary in these previous studies. SOCMEs calculated from Eq. (33) can therefore be regarded as more consistent from a formal point of view. This correctness, however, comes at the cost of solving the auxiliary second-order response equations, i.e., Eqs. (22) and (23), as well as a more elaborate evaluation needed for the diagonal terms of $\gamma^{NM}$. The resulting equations are in fact similar to those obtained in the early studies of Vahtras *et al.*,[18] safe for the DFT or BSE specific kernels and hyperkernels.

We note that the first-order matrix element

$$v_{0N}^{\eta,as} = \mathrm{Tr}\left(v_{ia} L_{ia}^N\right) \tag{37}$$

is correctly evaluated using the $\mathbf{L} = (\mathbf{X} - \mathbf{Y})$ part instead of the $\mathbf{R} = (\mathbf{X} + \mathbf{Y})$ part as suggested in Refs. 15–17. We stress that after a unitary transformation to the AO basis set, $(\mathbf{X} + \mathbf{Y})$ is symmetric, while the SOMF operator is skew-symmetric. Therefore, $\mathrm{Tr}\,(v_{\mu\nu}^{\mathrm{SOMF}}(X+Y)_{\mu\nu})$ actually vanishes for every excited state. Only within the Tamm–Dancoff approximation, where $\mathbf{Y} = 0$, this issue is rectified.

### C. State coupling using perturbative spin–orbit coupling

The state interaction between singlet and triplet excited states can be obtained from quasi-degenerate perturbation theory (QDPT) by means of an effective Hamiltonian[16]

$$\hat{H}_{\mathrm{rel}} = \hat{H}^0 + \hat{H}^{\mathrm{SOC}}. \tag{38}$$

The zeroth-order Hamiltonian $\hat{H}_0$ is a diagonal matrix,

$$\hat{H}^0 = \begin{pmatrix} 0 & & & \\ & \omega_N & & \\ & & \omega_M & \\ & & & \ldots \end{pmatrix}, \tag{39}$$

with zero representing the ground state, followed by the singlet and triplet excitation energies. We note that the $m_L = \{\pm 1, 0\}$ triplet excitation energies are still energetically degenerate in $\hat{H}_0$. The matrix elements of the spin–orbit coupling Hamiltonian are subsequently obtained from $v_{NM}^{\eta,\mathrm{SOMF}}$,

$$\hat{H}_{NM}^{\mathrm{SOC}} = \mathbf{S}\langle N|\hat{H}_\eta^{SO}|M\rangle = \mathbf{S}v_{NM}^{\eta,\mathrm{SOMF}}, \tag{40}$$

after a transformation from the Cartesian $\eta \in \{x, y, z\}$ into the spherical basis $\tilde{\eta} \in \{\pm 1, 0\}$ using the unitary transformation matrix,[42]

$$\mathbf{S} = \begin{pmatrix} \frac{1}{\sqrt{2}} & \frac{i}{\sqrt{2}} & 0 \\ \frac{-1}{\sqrt{2}} & \frac{i}{\sqrt{2}} & 0 \\ 0 & 0 & 1 \end{pmatrix}. \tag{41}$$

The selection rules for non-vanishing matrix elements are described in detail elsewhere.[16,17]

After the diagonalization of the Hamiltonian $\hat{H}_{\mathrm{rel}}$, the perturbed excited state energies $\widetilde{\omega}$ are obtained directly from the eigenvalues. Perturbed transition properties are subsequently evaluated similarly to Eq. (20) of Ref. 16. Using the perturbed eigenvector coefficients, $C_N^M$ and $D_{M,m_L}^N$, assigned to singlet and triplet parts of the eigenvectors obtained from $\hat{H}_{\mathrm{rel}}$ and $m_L = \{-1, 0, 1\}$, an explicit formula for perturbed transition properties can be obtained by projecting the unperturbed transition properties using the perturbed eigenvectors as

$$\widetilde{v}_{ij} = \underbrace{\sum_{N=0}^{N_s}\sum_{M=0}^{N_s} C_N^I C_M^J v_{NM}^{s-s}}_{\text{singlet part}} + \underbrace{\sum_{m_L}^{\pm 1,0}\sum_{N=1}^{N_t}\sum_{M=1}^{N_t} D_{N,m_L}^I D_{M,m_L}^J v_{NM}^{t-t}}_{\text{triplet part}}. \tag{42}$$

Equation (42) differs from previous results[16] only by realizing that the fully relaxed singlet–singlet and triplet–triplet transition properties $v_{NM}$ obtained from Eq. (31) or (33) are to be used.

If $I = 0$, only matrix elements $v_{0N}^{s-s}$ are needed for the first term in Eq. (42), as other contributions vanish due to the block structure of the effective Hamiltonian. At this point, we note that the *GW*–BSE method has issues with yielding good triplet excitation energies,[43] which cannot be avoided as soon as spin–orbit coupling is taken into account. Within this work, we will, however, neglect this issue as it impacts both one-component and two-component DFT and the *GW*–BSE method alike, as long as singlet and triplet parts can be assumed to be sufficiently distinguishable. If this is not the case, a more detailed re-investigation needs to be performed, although the perturbation theory introduced in this chapter is then no longer suited to be used anyways.

## III. PERTURBED EXCITED STATE PROPERTIES

Further properties can be evaluated from the corrected transition moments. To obtain SOC perturbed transition properties, the unperturbed transition property must be calculated for each singlet–singlet and triplet–triplet transition used in the construction of the effective SOC Hamiltonian and subsequently projected using Eq. (42). The main computational bottleneck is, however, the second-order Bethe–Salpeter response equations (22) and (23), which are independent of the actual transition property. Evaluating the expectation values over different transition properties is therefore negligible as is the projection from the unperturbed to the perturbed representation.

In this section, we will therefore shortly outline the SOC perturbed oscillator strength, the rotator strength, as well as the construction of a SOC perturbed transition matrix (T-matrix).[42]

While only oscillator strengths will be tested in this work, especially the T-matrix construction will become necessary to allow for an exploratory description of optical materials in an upcoming study currently being carried out in our laboratories.[44] The rotator strength is tightly linked to circular dichroism (CD) spectroscopy, which is also becoming increasingly important in the investigation and design of chiral optical materials.[45]

### A. Dipole transitions between excited states

The oscillator strength between two excited states can be obtained as

$$f_{IJ} = \frac{2\Delta\widetilde{\Omega}_{ij}}{3}|\widetilde{\mu}^{l}_{ij}|, \tag{43}$$

$$f_{IJ} = \frac{2}{3\Delta\widetilde{\Omega}_{ij}}|\widetilde{\mu}^{v}_{ij}|, \tag{44}$$

from the electric transition dipole moment $\widetilde{\mu}_{ij}$ in either its length or velocity representation. Furthermore, $\Delta\widetilde{\Omega}_{ij} = \widetilde{\omega}_I - \widetilde{\omega}_J$ denotes the difference between the excited states. These improved transition moments provide an excellent starting point for excited state dynamics in systems with significant spin–orbit coupling. Interconversion rates between the vibrational ground states of two excited states, $k^{r,0-0}_{I\to J}$, are subsequently obtained as[46,47]

$$k^{r,0-0}_{I\to J} = \frac{2\pi e^2}{\varepsilon_0 c^3 m_e h^2}\Delta\widetilde{\Omega}^2_{ij} f_{IJ}. \tag{45}$$

### B. Rotatory strength between excited states

The rotatory strength between two excited states can be calculated as

$$R^{\alpha\beta}_{ij} = \mathrm{Im}\left[\widetilde{\mu}^{\alpha}_{ij}\widetilde{m}^{\beta}_{ij}\right], \tag{46}$$

where $\alpha$ and $\beta$ refer to the respective Cartesian components, $\widetilde{\mu}_{ij}$ represents the perturbed electric transition dipole moment in either its length or velocity representation, and $\widetilde{m}_{ij}$ denotes the perturbed magnetic transition dipole moment. Only the latter is fully gauge invariant.[48] The rotatory strength is directly related to circular dichroism (CD) and optical rotation (OR) spectra. Both properties can be calculated from it using standard procedures.[48] The same holds true for the orientation-independent Hermitian optical rotation tensor,[49]

$$B^{\alpha\beta}_{ij} = \left[R^{\alpha\beta}_{ij} + R^{\beta\alpha}_{ij} + \frac{1}{3}A^{\alpha\beta}_{ij}\right], \tag{47}$$

where the electric dipole–electric quadrupole polarizability tensor $A$ is[50]

$$A^{\alpha\beta}_{ij} = \varepsilon_{\alpha\gamma\delta}\widetilde{\mu}^{\gamma}_{ij}\widetilde{\Theta}^{\delta\beta}_{ij} + \varepsilon_{\beta\gamma\delta}\widetilde{\mu}^{\beta}_{ij}\widetilde{\Theta}^{\delta\alpha}_{ij}, \tag{48}$$

where $\widetilde{\Theta}_{ij}$ denotes the perturbed electric quadrupole transition moment and $\varepsilon_{\alpha\beta\gamma}$ is the Levi–Cività symbol.

### C. Approximate perturbed T-matrices for excited states

T-matrix techniques have recently become rather popular in *ab initio* modeling of optical properties of materials starting from atomistic simulations. Those can be obtained in an approximate manner from a sum-over-state expansion as[42]

$$T^{m_l,n_l}_{I}(\omega) = \frac{ic_h Z_h k_h^3}{6\pi}\sum_{\alpha,\beta} S^{\alpha}_{m_l}(S^{\beta}_{n_l})^{-1} \times \sum_{N}\frac{\widetilde{v}^{\alpha}_{ij}\widetilde{v}^{\beta}_{ij}}{\Delta\widetilde{\Omega} - \omega + i\Gamma} + \sum_{N}\frac{\widetilde{v}^{\alpha}_{ij}\widetilde{v}^{\beta}_{ij}}{\Delta\widetilde{\Omega} + \omega - i\Gamma}, \tag{49}$$

where $c_h$ is the speed of light in the surrounding medium, $Z_h$ is the wave impedance, and $k_h$ is the wave number of the host material.[51] Note that these quantities are frequency dependent. **S** again denotes the Cartesian to spherical basis transformation coefficients, and $\Gamma$ is an imaginary broadening factor, preventing divergence in case $\Delta\widetilde{\Omega} = \omega$. The index $N$ formally runs over all perturbed excited states, which is unfeasible for sizable systems. A direct access of the perturbed excited state T-matrix would, however, require fourth-order response theory.

## IV. COMPUTATIONAL METHODS

To outline the capabilities of calculating excited state properties using the BSE, we investigate the excited state absorption (ESA) spectra of the dipyrromethene boron difluoride (BODIPY) derivative pyrromethene-567 (PM567)[52] and the well-known bipyridine (bpy) $[Ru(bpy)_3]^{2+}$ complex of ruthenium.[53] Furthermore, we put the perturbative spin–orbit coupling approach to test with the demanding mercaptoaryl-oxazoline complex [PdI(S-phoz)(IMes)],[54] for whose spectral features have been shown to strongly depend on SOC,[23] and with the $[Ir(ppy)_2(sip)]^+$ complex featuring a 5d metal center.[55] The geometries of the metal complexes were optimized using the BP86[56,57] functional with the def2-SVP basis set.[58] For the geometry optimizations, the ECP28MWB (Pd, Ru, I) and ECP60MWB (Ir) effective core potentials were used.[59] For PM567, the respective geometries reported in Ref. 60 were used. Subsequent scalar-relativistic (time-dependent) PBE0,[61,62] $G_0W_0$@PBE0, eigenvalue self-consistent $GW$@PBE0 (ev$GW$@PBE0), and BSE calculations were performed using the all-electron x2c-TZVPPall basis set.[63] Reference two-component calculations were performed using the x2c-TZVPPall-2c basis set.[63] The auxiliary basis set reported in Ref. 63 together with the basis sets has been used in all ground state, $GW$, BSE, and TD-DFT calculations. Ground states were tightly converged to errors of less than $10^{-8}$ hartree in energy and differences in the densities of less than $10^{-7}$. A grid of size 3 was used in DFT calculations.[64,65] A seminumerical exchange algorithm was used to accelerate DFT calculations in combination with a very fine grid.[66] For the $G_0W_0$ and ev$GW$ calculations, the highest 10/20 occupied and lowest 10/20 unoccupied orbitals (1c)/spinors (2c) were optimized, and the remaining orbitals/spinors were shifted. The exact two-component (X2C) transformation was used to include relativistic effects.[67,68] Note that ten spatial orbitals equal 20 spinors for closed shell systems. Quasiparticle equations in ev$GW$ were considered converged if the change of HOMO and LUMO was lower than $10^{-5}$ hartree. To evaluate excited state properties, for each molecular

system, the first 16 singlet and triplet excited states were determined. Subsequently, all excited state transition moments between these states are calculated to yield the excited state absorption spectra. In case of perturbative spin–orbit coupling, the coupling matrix was also constructed from the same 16 singlet and triplet states in addition to the singlet ground states. Due to the high numerical effort, 2c BSE calculations were carried out using two NVIDIA A100 GPUs to accelerate the construction of matrix–vector products.[69] All plotted spectra were obtained by applying a broadening of 0.05 eV full width at half maximum (FWHM). Oscillator strengths were obtained in the length gauge throughout this work.

To predict transient absorption spectra, at a given geometry, first the ground state absorption spectra need to be calculated in any case. Subsequently, from excitation vectors of the ground state absorption amplitudes, the excited state absorption amplitudes are evaluated as outlined in Sec. II A. De-excitations from the excited state are assumed to be inverse excitations and, therefore, have the same absolute excitation energy, but reversed signs for both energy and oscillator strength. All absorption cross sections are given in atomic units (a.u.) and can be converted to molar absorption coefficients in $\frac{L}{mol \cdot cm}$ using the constant $a_0^2 \cdot N_{\mathrm{Avogadro}} \cdot 10 \approx 16\,836.7$.

All calculations were performed using a development version of Turbomole V7.9.[70,71]

## V. RESULTS AND DISCUSSION

### A. $[Ru(bpy)_3]^{2+}$

The tris(bipyridine)ruthenium(II) dication $[Ru(bpy)_3]^{2+}$ is one of the most well-known optically active complexes, with optical investigations dating back nearly three decades.[53] The simulated TD-PBE0 and ev*GW*–BSE absorption spectra are outlined in Fig. 1. ev*GW*–BSE is in very good agreement with the experimental measurements of Yersin *et al.*,[53] who found the lowest energy band starting at ~2.73 eV (22 000 $cm^{-1}$). This band is assumed to be a metal–ligand charge-transfer (MLCT) band and interestingly found

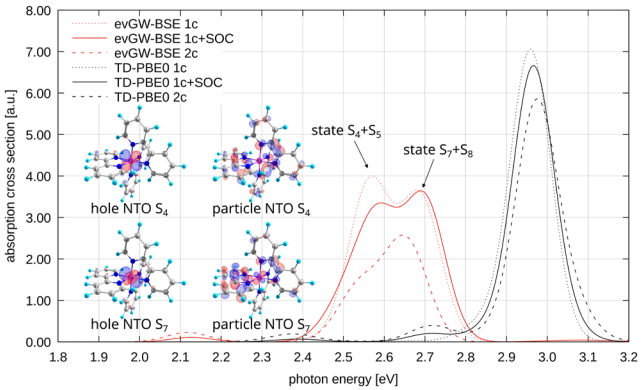


**FIG. 1.** Ground state absorption spectra of $[Ru(bpy)_3]^{2+}$ obtained from scalar relativistic (1c, dotted line), scalar relativistic plus perturbative spin–orbit coupling (1c+SOC, solid line), and fully relativistic two-component (2c, dashed line) spectra obtained from ev*GW*–BSE and TD-PBE0. An arbitrary broadening of 0.05 eV is applied. Absorption cross section given in atomic units (a.u.). The inset shows the natural transition orbitals (NTOs) of the main peaks, calculated for ev*GW*–BSE.

at a too high energy when TD-PBE0 is used. This is in line with earlier observations that already 20% of HF exchange found in B3LYP is sufficient to shift the MLCT band to the correct position.[72] Only for pure density functionals, as for example BP86, the typical strong underestimation of charge-transfer excitations is observed.[72] Both TD-PBE0 and ev*GW*–BSE predict this band to be composed of two excited states, with ev*GW*–BSE and TD-PBE0, however, yielding distinctly different oscillator strengths. A comparison of the 1c and 2c methods reveals that these principal absorption bands defining the visible part of the $[Ru(bpy)_3]^{2+}$ spectrum are only moderately influenced by spin–orbit coupling. At low temperatures, an additional emission band at lower energy is observed. This band is assigned to a triplet excited state[53] and can therefore only be modeled if spin–orbit coupling is included. This is experimentally observed at 17 684 $cm^{-1}$[53] and clearly belongs to the weal transition predicted by both ev*GW*–BSE and TD-PBE0, as long as spin–orbit coupling is taken into account. Figure 1 overall outlines that our implemented perturbative approach is in good agreement with the full 2c methods for $[Ru(bpy)_3]^{2+}$. Both excitation energy and oscillator strength of the triplet band are well reproduced.

Given the availability and stability of $[Ru(bpy)_3]^{2+}$, it is one of the few compounds where experimental excited state absorption data are also available.[73,74] The inset in Fig. 1 shows the labeling of the calculated main absorption peaks at 2.56 and 2.69 eV. These correspond to excited states $S_4$ and $S_7$ in our calculation and have nearly degenerate partners in both energy and oscillator strength, constituting excited states $S_5$ and $S_8$. These states align well with the findings of Ref. 75, who have used polarized emission spectra to assign the symmetry of the main component as belonging to the $E'$ IRREP in point group $D_3$, i.e., being doubly degenerate. The natural transition orbital (NTO) analysis shown as the inset of Fig. 1 confirms that especially excited state $S_4$ is a pure MLCT transition and state $S_5$ was confirmed to be symmetry related, too. We therefore assume that state $S_4$ is the (dipole allowed) main experimentally observed MLCT absorption and emission state.[75] For TD-PBE0, we find that states $S_5/S_6$ and $S_7/S_8$ correspond to the two degenerate pairs described for ev*GW*–BSE. These two degenerate pairs are energetically close to each other, fusing into a single peak in Fig. 1. The state ordering and oscillator strength distribution of ev*GW* further aligns well with the obtained MS-CASPT2 values of Atkins *et al.*[72] ev*GW*, like MS-CASPT2, predicts three nearly dark states followed by two energetically degenerate bright states 4 and 5, and again bright states $S_7$ and $S_8$ that are approximately of the same oscillator strength. Contrary, TD-B3LYP and TD-PBE0 predict states $S_5$ and $S_6$ to be nearly dark, and only $S_7$ and $S_8$ to have a significant oscillator strength.[72]

Hauser and Krausz found the first excited state absorption peak for the MLCT excited state at ~1.2 eV (10 000 $cm^{-1}$), as shown in Fig. 2 of Ref. 74. This first excitation peak is well reproduced by ev*GW*–BSE as shown in the predicted transient absorption spectra [Fig. 2]. In addition, both ev*GW*–BSE and TD-PBE0 hint at excited state absorption being also important in the infrared region below 0.5 eV, although no experimental data are available in this range, as the mentioned Fig. 2 of Ref. 74 only reports absorption starting from 5000 $cm^{-1}$ (0.62 eV). Contrary to the ground state, spin–orbit coupling is important to correctly describe the ESA amplitude of the MLCT band in this complex, marked using red lines in Figs. 2 and 3. While the peak positions nearly perfectly align, large deviations

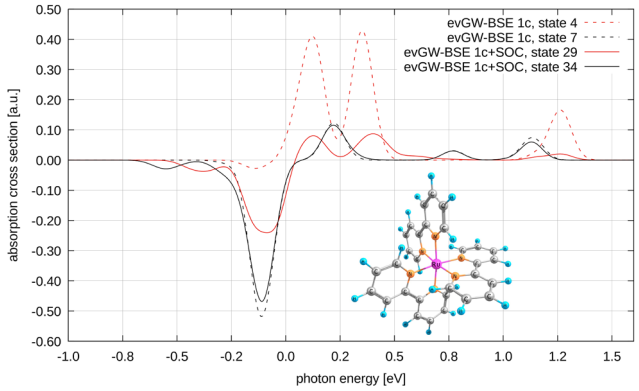


**FIG. 2.** Predicted transient absorption spectra of $[Ru(bpy)_3]^{2+}$ obtained from scalar relativistic (1c, dotted line) and scalar relativistic plus perturbative spin–orbit coupling (1c+SOC, solid line) spectra obtained from ev*GW*–BSE. Negative oscillator strengths correspond to emission lines. An arbitrary broadening of 0.05 eV is applied. The absorption cross section at 0.0 eV is an artifact of this broadening. Absorption cross section given in atomic units (a.u.). Note that the degenerate states 5/30 and 8/34 yield identical results.

in the predicted oscillator strengths can be found for ev*GW*–BSE. For TD-PBE0, the predicted transient absorption spectra with and without spin–orbit coupling closely resemble each other in the absorption regime above 0.0 eV. Below 0.0 eV, both ev*GW*–BSE and TD-PBE0 behave distinctly different if spin–orbit coupling is turned on, outlining that singlet–triplet transitions are rather important, as expected. In contrast, for the higher-lying excited state of $E'$ symmetry, marked using black lines in Figs. 2 and 3, SOC is only important in the de-excitation regime, where intersystem crossing can lead to a lower-lying triplet state, which is strictly forbidden without spin–orbit coupling. Intersystem crossing is therefore a viable pathway for all bright excited states of $[Ru(bpy)_3]^{2+}$. When targeting intersystem crossing (ISC) specifically, we remind the reader that *GW*–BSE has issues with describing triplet states, which are often found at too low energy compared to singlet states. This is also true for many DFT functionals, including PBE0. It is therefore likely that the redshift of the negative peaks is too pronounced in Figs. 2 and 3. As mentioned earlier, other methods such as, for example, correlation-kernel-augmented BSE[76] could be used to specifically check for shifts in the triplet energies.

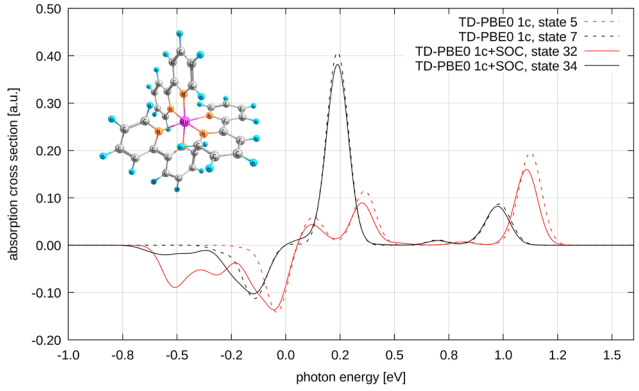


**FIG. 3.** Predicted transient absorption spectra of $[Ru(bpy)_3]^{2+}$ obtained from scalar relativistic (1c, dotted line) and scalar relativistic plus perturbative spin–orbit coupling (1c+SOC, solid line) spectra obtained from TD-PBE0. Negative oscillator strengths correspond to emission lines. An arbitrary broadening of 0.05 eV is applied. The absorption cross section at 0.0 eV is an artifact of this broadening. Absorption cross section given in atomic units (a.u.). Note that the degenerate states 6/33 and 8/34 yield identical results.

## B. BODIPY derivative PM567

The dipyrromethene boron difluoride (BODIPY) derivatives represent common cases that are usually not well described by TD-DFT.[77] We therefore turn to the PM567 BODIPY variant, for which an excitation energy of 2.22 eV has been found experimentally,[78] while XMC-QDPT2 predicts 2.13 eV. As outlined in Fig. 4, ev*GW*–BSE is in excellent agreement with these findings, yielding an excitation energy of 2.29 eV, while $G_0W_0$–BSE underestimates and TD-PBE0 overestimates these values. Recently, Valiev *et al.*[79,80] have also investigated the excited state properties of this system, especially focused on intersystem crossing and internal conversion effects. They consider Duschinsky, anharmonic, and Herzberg–Teller effects. While we will not dive into these effects in detail, still another important detail can be observed in our simulations, namely, the dependence of the BSE spectrum on the underlying *GW* spectrum. As shown in Fig. 4, TD-PBE0 1c and 2c results are nearly identical, i.e., spin–orbit effects are not too important in the absorption spectrum of PM567. For the *GW* methods, 1c and 2c results in contrast differ, with small deviations in the peak positions and significant deviations in the obtained oscillator strengths. This can be attributed to the *GW* step carried out before the actual BSE calculation. As all orbitals enter the construction of the polarizability, the core orbital is already significantly influenced by spin–orbit coupling, leading to non-negligible differences. While this effect is less important for $G_0W_0$, i.e., the HOMO–LUMO gaps between 1c and 2c $G_0W_0$ differ by less than 0.01 eV, the effect is

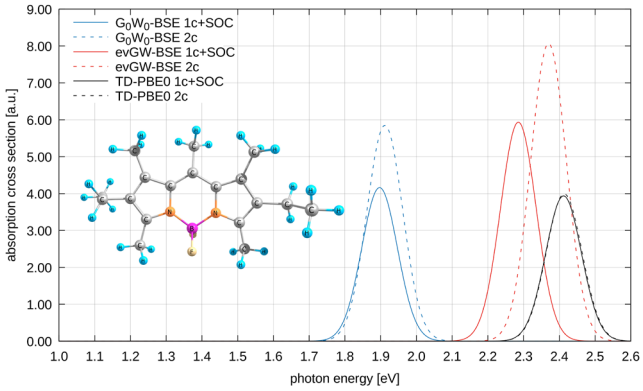


**FIG. 4.** Ground state absorption spectra of the BODIPY derivative PM567 obtained from scalar relativistic (1c, dotted line), scalar relativistic plus perturbative spin–orbit coupling (1c+SOC, solid line), and fully relativistic two-component (2c, dashed line) spectra obtained from $G_0W_0$–BSE, ev*GW*–BSE, and TD-PBE0. An arbitrary broadening of 0.05 eV is applied. Absorption cross section given in atomic units (a.u.).

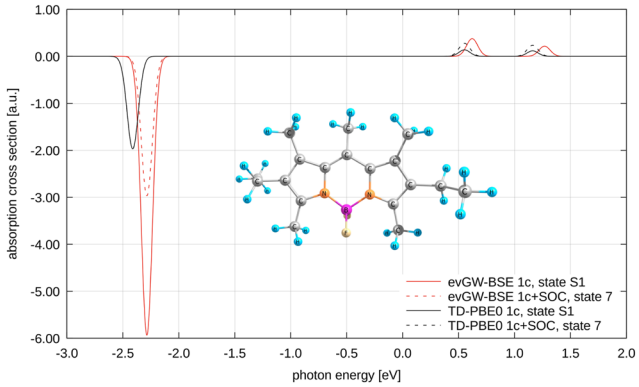


**FIG. 5.** Predicted transient absorption spectra of the BODIPY derivative PM567 obtained from scalar relativistic (1c, dotted line) and scalar relativistic plus perturbative spin–orbit coupling (1c+SOC, solid line) spectra obtained from ev*GW*–BSE. Negative oscillator strengths correspond to emission lines. An arbitrary broadening of 0.05 eV is applied. Absorption cross section given in atomic units (a.u.).

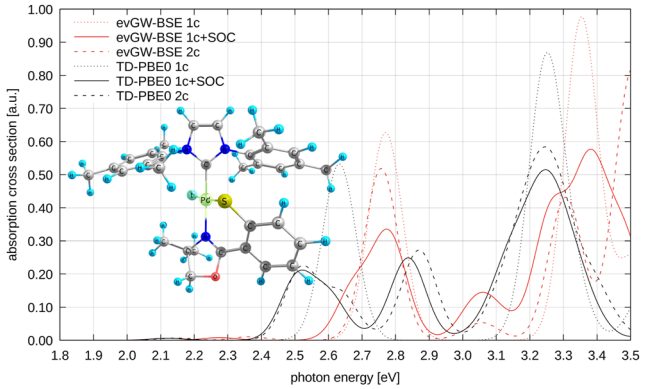


**FIG. 6.** Ground state absorption spectra of [PdI(S-phoz)] obtained from scalar relativistic (1c, dotted line), scalar relativistic plus perturbative spin–orbit coupling (1c+SOC, solid line), and fully relativistic two-component (2c, dashed line) spectra obtained from ev*GW*–BSE and TD-PBE0. An arbitrary broadening of 0.05 eV is applied. Absorption cross section given in atomic units (a.u.).

more pronounced for ev*GW*. For the latter, the HOMO–LUMO gap is widened by 0.05 eV when variational spin–orbit coupling is included. This shift is subsequently carried over to the BSE step and cannot be corrected by the perturbative SOC correction, as it is already included in the zeroth-order Hamiltonian $\hat{H}^0$ of Eq. (38). The resulting 1c+SOC results therefore closely resemble the plain 1c results, similar to TD-PBE0. Subsequent deviations in the oscillator strengths arising from the different screening in $\mathbf{W}$[23] are even more pronounced. This effect is especially strong for PM567, but in line with earlier observations on the dependence of the BSE oscillator strengths on the underlying *GW* method.[81] We note that setting the spin–orbit operator to zero in the 2c calculation leads to a perfect alignment of the 1c and 2c spectra, and we are therefore confident in the numerical validity of the results shown in Fig. 4.

Figure 5 further outlines that SOC effects cannot be identified as the main reason of the observed intersystem crossing in PM567, with no peak being visible between the $S_0 \rightarrow S_1$ transition. SOC effects on the 0–0 transitions are therefore vanishing, and ISC is dominated by Franck–Condon and Herzberg–Teller effects as outlined in the literature.[79,80]

### C. [PdI(S-phoz)(IMes)]

The mercaptoaryl-oxazoline complex [PdI(S-phoz)(IMes)][54] has been previously investigated by TD-PBE0 and *GW*–BSE,[23] and it was concluded that especially the spectrum of the halogenated iodine variant can only be correctly described with SOC being included. It therefore constitutes an excellent test for the perturbative SOC approach outlined in Sec. II B. As shown in Fig. 6, the effects of SOC are substantial. The uncorrected 1c spectrum barely has any resemblance to the full 2c spectrum. For example, scalar relativistic TD-PBE0 predicts a single peak at 2.63 eV. After turning on SOC, this peak is split into two major bands located from 2.4 to 3.0 eV with reduced oscillator strengths. Yet, the perturbative SOC procedure is able to largely incorporate this band shape. In the predicted 1c+SOC spectrum, the peak positions are both re-adjusted and the oscillator strengths accordingly redistributed. This leads to the observed excellent match between the full and perturbative SOC spectra for TD-PBE0. ev*GW*–BSE is more problematic within the perturbative SOC approach, as a too low-lying triplet state artificially mixes with a singlet state of similar energy at ~2.7 eV, with the triplet subsequently stealing intensity from the bright singlet peak observed in the other two ev*GW*–BSE spectra. 2c ev*GW*–BSE reveals that the triplet state in question is redshifted by about 0.3 eV. [PdI(S-phoz)(IMes)] is a prime example of the importance of SOC to recover the correct spectrum in cases where $S_n$–$T_n$ gaps are not too small. However, it also outlines a possible deterioration of the results if artificial singlet–triplet mixing of states that should not be close occurs, as in the ev*GW*–BSE spectrum.

### D. $[Ir(ppy)_2(sip)]^+$

As a final molecular test system, we consider a 2-phenylpyridine (ppy) complex of iridium, namely the $[Ir(ppy)_2(sip)]^+$ molecule.[55] This complex has a notable two-photon absorption cross section, making it an ideal candidate for theoretical testing in this direction. Similarly to its parent, the $[Ir(ppy)_3]$ complex, it features broad absorption bands with centers at 2.65 eV (468 nm), 3.07 (404 nm), and 3.40 eV (365 nm) that have been assigned to a series of metal–ligand charge-transfer states.[82] Figure 7 outlines that including spin–orbit coupling only slightly alters the overall shape of the absorption spectrum. In particular, TD-PBE0 closely resembles the experimental spectrum described in Ref. 55, yielding peaks close to the experimental reference values, with only minor differences between 1c, 1c+SOC, and full 2c spectra. Most prominent differences can again be found in the lowest energy part, where a transition to the triplet excited state is strictly forbidden in the 1c calculation, while 1c+SOC and 2c yield rather similar finite oscillator strengths. For ev*GW*, the differences between the 1c and 2c spectra are pronounced, which we again attribute to changes in the principal gap stemming from the *GW* procedure, which is not corrected by the perturbative SOC step.

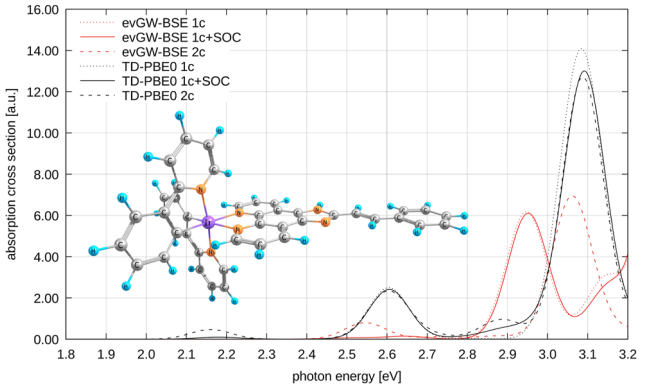


**FIG. 7.** Ground state absorption spectra of $[Ir(ppy)_2(sip)]^+$ obtained from scalar relativistic (1c, dotted line), scalar relativistic plus perturbative spin–orbit coupling (1c+SOC, solid line), and fully relativistic two-component (2c, dashed line) spectra obtained from ev*GW*–BSE and TD-PBE0. An arbitrary broadening of 0.05 eV is applied. Absorption cross section given in atomic units (a.u.).

However, Fig. 7 tends to oversimplify the complexity of the bands. While indeed the shape is similar or even nearly identical as for TD-PBE0, many more excited states will actually contribute to the band due to state mixing. However, the overall intensity is not significantly changed, as these contributions average out after the Gaussian peak broadening is applied. Earlier investigations of the $[Ir(ppy)_3]$ complex using quasi-degenerate perturbation theory at the DFT/MRCI level came to the same conclusion, finding a significant amount of state mixing.[83] This is not too surprising, given that the 5d iridium center promotes SOC. Distinct to the [PdI(S-phoz) (IMes)] complex discussed in Sec. V C, the $S_n$–$T_n$ gaps in $[Ir(ppy)_2(sip)]^+$ and $[Ir(ppy)_3]$ only amount to a few 100 $cm^{-1}$. A mixing of these states is therefore to be expected, although it barely affects the overall intensity of the bands, leading to the partially incorrect impression that SOC is not too important for these iridium complexes.

## VI. CONCLUSION

We have derived an efficient way to calculate excited state properties, including perturbative spin–orbit corrections for the *GW*–Bethe–Salpeter equation method. These advancements allow for the calculation of excited state absorption as well as other excited state properties as, for example, excited state circular dichroism, optical rotation, or T-matrices for multiscale modeling.[44,51,84] Furthermore, using the same route, perturbative spin–orbit coupling corrections can be obtained for both ground and excited state spectra. While we focused on the *GW*–BSE method, we also outlined the necessary modifications needed to extend perturbative spin–orbit coupling to excited state properties within time-dependent DFT. Given the broad availability of TD-DFT, this adaption can be useful to enhance existing codes.

To demonstrate the capabilities of our BSE excited state property implementation, we have investigated four sizable molecular systems. First, it could be shown that excited state absorption is well described by our *GW*–BSE implementation, closely following experimentally observed features in $[Ru(bpy)_3]^2$. Next, it could be shown that including SOC is straightforward for TD-DFT and leads to excellent agreement with fully relativistic 2c TD-DFT calculations. For *GW*–BSE, the situation is more complex when perturbative SOC is to be included. The perturbative SOC treatment only recovers state interactions from the BSE part but does not correct for differences entering the zeroth-order Hamiltonian through differences in the quasiparticle energies obtained from the respective 1c and 2c *GW* methods. Further corrections would be needed to fully align 1c and 2c *GW*–BSE methods, although the differences are usually well within the errors of obtained excitation energies and oscillator strengths.[5,81,85] The conclusion of Ref. 81, stating that a more detailed evaluation of the dependence of excited state properties on the underlying DFT functional as well as the details of the *GW* method needs to be carried out, is underlined by our results

## SUPPLEMENTARY MATERIAL

Standard xyz files with the optimized structures, machine readable ASCII files listing all excited states and oscillator strengths used to generate Figs. 1–7, and two example inputs for $H_2O$ and $[Ru(bpy)_3]^{2+}$ are contained in the supplementary material. Singlet–singlet transition moments can be found in the file transmom_s2s, triplet–triplet transition moments in transmom_t2t, and the perturbatively spin–orbit coupled moments in transmom_soc.

## ACKNOWLEDGMENTS

C.H. acknowledges the Volkswagen Stiftung for the financial support.

## AUTHOR DECLARATIONS

### Conflict of Interest

The authors have no conflicts to disclose.

### Author Contributions

**Paula Himmelsbach**: Conceptualization (equal); Data curation (equal); Investigation (equal); Methodology (equal); Software (lead); Validation (equal); Visualization (equal); Writing – original draft (supporting); Writing – review & editing (supporting). **Christof Holzer**: Conceptualization (equal); Data curation (equal); Formal analysis (equal); Investigation (equal); Methodology (equal); Software (supporting); Validation (equal); Visualization (equal); Writing – original draft (lead); Writing – review & editing (lead).

## DATA AVAILABILITY

The data that support the findings of this study are available within the article and its supplementary material.

## REFERENCES

[1] I. Knysh, J. D. J. Villalobos-Castro, I. Duchemin, X. Blase, and D. Jacquemin, Phys. Chem. Chem. Phys. **25**, 29993 (2023).
[2] N. Rauwolf, W. Klopper, and C. Holzer, J. Chem. Phys. **160**, 061101 (2024).
[3] J. Villalobos-Castro, I. Knysh, D. Jacquemin, I. Duchemin, and X. Blase, J. Chem. Phys. **159**, 024116 (2023).

[4]X. Blase and C. Attaccalite, Appl. Phys. Lett. **99**, 171909 (2011).
[5]X. Gui, C. Holzer, and W. Klopper, J. Chem. Theory Comput. **14**, 2127 (2018).
[6]X. Blase, I. Duchemin, D. Jacquemin, and P.-F. Loos, J. Phys. Chem. Lett. **11**, 7371 (2020).
[7]Y. Cho, S. J. Bintrim, and T. C. Berkelbach, J. Chem. Theory Comput. **18**, 3438 (2022).
[8]J. Li, D. Golze, and W. Yang, J. Chem. Theory Comput. **18**, 6637 (2022).
[9]Y. Yao, D. Golze, P. Rinke, V. Blum, and Y. Kanai, J. Chem. Theory Comput. **18**, 1569 (2022).
[10]P.-F. Loos and X. Blase, J. Chem. Phys. **153**, 114120 (2020).
[11]S. J. Bintrim and T. C. Berkelbach, J. Chem. Phys. **156**, 044114 (2022).
[12]P.-F. Loos and P. Romaniello, J. Chem. Phys. **156**, 164101 (2022).
[13]E. Monino and P.-F. Loos, J. Chem. Theory Comput. **17**, 2852 (2021).
[14]L. Zhendong, S. Bingbing, Z. Yong, X. Yunlong, and L. Wenjian, Mol. Phys. **111**, 3741 (2013).
[15]X. Gao, S. Bai, D. Fazzi, T. Niehaus, M. Barbatti, and W. Thiel, J. Chem. Theory Comput. **13**, 515 (2017).
[16]B. de Souza, G. Farias, F. Neese, and R. Izsák, J. Chem. Theory Comput. **15**, 1896 (2019).
[17]C. Liao, J. M. Kasper, A. J. Jenkins, P. Yang, E. R. Batista, M. J. Frisch, and X. Li, JACS Au **3**, 358 (2023).
[18]O. Vahtras, H. Ågren, P. Jo/rgensen, H. Jo/rgen Aa Jensen, T. Helgaker, and J. Olsen, J. Chem. Phys. **96**, 2118 (1992).
[19]M. Rohlfing and S. G. Louie, Phys. Rev. Lett. **80**, 3320 (1998).
[20]C. Faber, P. Boulanger, I. Duchemin, C. Attaccalite, and X. Blase, J. Chem. Phys. **139**, 194308 (2013).
[21]X. Blase, I. Duchemin, and D. Jacquemin, Chem. Soc. Rev. **47**, 1022 (2018).
[22]K. Krause and W. Klopper, J. Comput. Chem. **38**, 383 (2017).
[23]C. Holzer, A. M. Teale *et al.*, J. Chem. Phys. **150**, 214112 (2019).
[24]R. Bauernschmitt and R. Ahlrichs, Chem. Phys. Lett. **256**, 454 (1996).
[25]R. Bauernschmitt and R. Ahlrichs, J. Chem. Phys. **104**, 9047 (1996).
[26]C. Holzer, J. Chem. Theory Comput. **19**, 3131 (2023).
[27]S. M. Parker, D. Rappoport, and F. Furche, J. Chem. Theory Comput. **14**, 807 (2018).
[28]F. Furche, J. Chem. Phys. **114**, 5982 (2001).
[29]M. van Schilfgaarde, T. Kotani, and S. Faleev, Phys. Rev. Lett. **96**, 226402 (2006).
[30]T. Kotani, M. Van Schilfgaarde, and S. V. Faleev, Phys. Rev. B **76**, 165106 (2007).
[31]J. E. Bates and F. Furche, J. Chem. Phys. **137**, 164105 (2012).
[32]C. Holzer, Y. J. Franzke, and M. Kehry, J. Chem. Theory Comput. **17**, 2928 (2021).
[33]A. Pausch and C. Holzer, J. Phys. Chem. Lett. **13**, 4335 (2022).
[34]C. Holzer, Y. J. Franzke, and A. Pausch, J. Chem. Phys. **157**, 204102 (2022).
[35]S. Yamada, Y. Noguchi, K. Ishii, D. Hirose, O. Sugino, and K. Ohno, Phys. Rev. B **106**, 045113 (2022).
[36]E. Monino and P.-F. Loos, J. Chem. Phys. **159**, 034105 (2023).
[37]C. Holzer and W. Klopper, J. Chem. Phys. **149**, 101101 (2018).
[38]E. C. Alguire, Q. Ou, and J. E. Subotnik, J. Phys. Chem. B **119**, 7140 (2015).
[39]Q. Ou, E. C. Alguire, and J. E. Subotnik, J. Phys. Chem. B **119**, 7150 (2015).
[40]B. A. Heß, C. M. Marian, U. Wahlgren, and O. Gropen, Chem. Phys. Lett. **251**, 365 (1996).
[41]B. Helmich-Paris, C. Hättig, and C. van Wüllen, J. Chem. Theory Comput. **12**, 1892 (2016).
[42]I. Fernandez-Corbaton, D. Beutel, C. Rockstuhl, A. Pausch, and W. Klopper, ChemPhysChem **21**, 878 (2020).
[43]D. Jacquemin, I. Duchemin, A. Blondel, and X. Blase, J. Chem. Theory Comput. **13**, 767 (2017).
[44]B. Zerulla, D. Beutel, C. Holzer, I. Fernandez-Corbaton, C. Rockstuhl, and M. Krstić, Adv. Mater. **36**, 2311405 (2024).
[45]L. Rebholz, M. Krstić, B. Zerulla, M. Pawlak, W. Lewandowski, I. Fernandez-Corbaton, and C. Rockstuhl, ACS Photonics **11**, 1771 (2024).
[46]S. Haneder, E. Da Como, J. Feldmann, J. M. Lupton, C. Lennartz, P. Erk, E. Fuchs, O. Molt, I. Münster, C. Schildknecht, and G. Wagenblast, Adv. Mater. **20**, 3325 (2008).
[47]M. Kühn and F. Weigend, J. Chem. Phys. **141**, 224302 (2014).
[48]I. Warnke and F. Furche, WIREs Comput. Mol. Sci. **2**, 150 (2012).
[49]A. D. Buckingham and M. B. Dunn, J. Chem. Soc. A **1971**, 1988.
[50]J. Autschbach, ChemPhysChem **12**, 3224 (2011).
[51]B. Zerulla, M. Krstić, D. Beutel, C. Holzer, C. Wöll, C. Rockstuhl, and I. Fernandez-Corbaton, Adv. Mater. **34**, 2200350 (2022).
[52]A. Costela, I. García-Moreno, C. Gomez, R. Sastre, F. Amat-Guerri, M. Liras, F. López Arbeloa, J. Bañuelos Prieto, and I. López Arbeloa, J. Phys. Chem. A **106**, 7736 (2002).
[53]H. Yersin, W. Humbs, and J. Strasser, Coord. Chem. Rev. **159**, 325 (1997).
[54]C. Holzer, A. Dupé, L. M. Peschel, F. Belaj, and N. C. Mösch-Zanetti, Eur. J. Inorg. Chem. **2018**, 568.
[55]X.-D. Bi, R. Yang, Y.-C. Zhou, D. Chen, G.-K. Li, Y.-X. Guo, M.-F. Wang, D. Liu, and F. Gao, Inorg. Chem. **59**, 14920 (2020).
[56]A. D. Becke, Phys. Rev. A **38**, 3098 (1988).
[57]J. P. Perdew, Phys. Rev. B **33**, 8822 (1986).
[58]F. Weigend, Phys. Chem. Chem. Phys. **8**, 1057 (2006).
[59]D. Andrae, U. Häußermann, M. Dolg, H. Stoll, and H. Preuß, Theor. Chim. Acta **77**, 123 (1990).
[60]R. R. Valiev, V. N. Cherepanov, G. V. Baryshnikov, and D. Sundholm, Phys. Chem. Chem. Phys. **20**, 6121 (2018).
[61]J. P. Perdew, K. Burke, and M. Ernzerhof, Phys. Rev. Lett. **77**, 3865 (1996).
[62]C. Adamo and V. Barone, J. Chem. Phys. **110**, 6158 (1999).
[63]P. Pollak and F. Weigend, J. Chem. Theory Comput. **13**, 3696 (2017).
[64]O. Treutler, "Entwicklung und Anwendung von Dichtefunktionalmethoden," Dr. rer. nat. Dissertation (University of Karlsruhe, TH, Germany, 1995).
[65]O. Treutler and R. Ahlrichs, J. Chem. Phys. **102**, 346 (1995).
[66]C. Holzer, J. Chem. Phys. **153**, 184115 (2020).
[67]D. Peng, N. Middendorf, F. Weigend, and M. Reiher, J. Chem. Phys. **138**, 184105 (2013).
[68]Y. J. Franzke, N. Middendorf, and F. Weigend, J. Chem. Phys. **148**, 104410 (2018).
[69]Y. J. Franzke, C. Holzer, and F. Mack, J. Chem. Theory Comput. **18**, 1030 (2022).
[70]Y. J. Franzke, C. Holzer, J. H. Andersen, T. Begušić, F. Bruder, S. Coriani, F. Della Sala, E. Fabiano, D. A. Fedotov, S. Fürst, S. Gillhuber, R. Grotjahn, M. Kaupp, M. Kehry, M. Krstić, F. Mack, S. Majumdar, B. D. Nguyen, S. M. Parker, F. Pauly, A. Pausch, E. Perlt, G. S. Phun, A. Rajabi, D. Rappoport, B. Samal, T. Schrader, M. Sharma, E. Tapavicza, R. S. Treß, V. Voora, A. Wodyński, J. M. Yu, B. Zerulla, F. Furche, C. Hättig, M. Sierka, D. P. Tew, and F. Weigend, J. Chem. Theory Comput. **19**, 6859 (2023).
[71]S. G. Balasubramani, G. P. Chen, S. Coriani, M. Diedenhofen, M. S. Frank, Y. J. Franzke, F. Furche, R. Grotjahn, M. E. Harding, C. Hättig, A. Hellweg, B. Helmich-Paris, C. Holzer, U. Huniar, M. Kaupp, A. Marefat Khah, S. Karbalaei Khani, T. Müller, F. Mack, B. D. Nguyen, S. M. Parker, E. Perlt, D. Rappoport, K. Reiter, S. Roy, M. Rückert, G. Schmitz, M. Sierka, E. Tapavicza, D. P. Tew, C. van Wüllen, V. K. Voora, F. Weigend, A. Wodyński, and J. M. Yu, J. Chem. Phys. **152**, 184107 (2020).
[72]A. J. Atkins, F. Talotta, L. Freitag, M. Boggio-Pasqua, and L. González, J. Chem. Theory Comput. **13**, 4123 (2017).
[73]S. J. Milder, J. S. Gold, and D. S. Kliger, Chem. Phys. Lett. **144**, 269 (1988).
[74]A. Hauser and E. Krausz, Chem. Phys. Lett. **138**, 355 (1987).

[75]H. Yersin and E. Gallhuber, J. Am. Chem. Soc. **106**, 6582 (1984).
[76]C. Holzer and W. Klopper, J. Chem. Phys. **147**, 181101 (2017).
[77]M. R. Momeni and A. Brown, J. Chem. Theory Comput. **11**, 2619 (2015).
[78]R. Valiev, A. Sinelnikov, Y. Aksenova, R. Kuznetsova, M. Berezin, A. Semeikin, and V. Cherepanov, Spectrochim. Acta, Part A **117**, 323 (2014).
[79]R. R. Valiev, V. N. Cherepanov, R. T. Nasibullin, D. Sundholm, and T. Kurten, Phys. Chem. Chem. Phys. **21**, 18495 (2019).
[80]R. R. Valiev, B. S. Merzlikin, R. T. Nasibullin, A. Kurtzevitch, V. N. Cherepanov, R. R. Ramazanov, D. Sundholm, and T. Kurtén, Phys. Chem. Chem. Phys. **25**, 6406 (2023).
[81]D. Jacquemin, I. Duchemin, A. Blondel, and X. Blase, J. Chem. Theory Comput. **12**, 3969 (2016).
[82]T. Hofbeck and H. Yersin, Inorg. Chem. **49**, 9290 (2010).
[83]M. Kleinschmidt, C. van Wüllen, and C. M. Marian, J. Chem. Phys. **142**, 094301 (2015).
[84]B. Zerulla, C. Li, D. Beutel, S. Oßwald, C. Holzer, J. Bürck, S. Bräse, C. Wöll, I. Fernandez-Corbaton, L. Heinke, C. Rockstuhl, and M. Krstić, Adv. Funct. Mater. **34**, 2301093 (2023).
[85]D. Jacquemin, I. Duchemin, and X. Blase, J. Chem. Theory Comput. **11**, 5340 (2015).